Revealing the band structure of InSb nanowires by high-field magnetotransport in the quasiballistic regime

Florian Vigneau,[1] Önder Gül,[2] Yann-Michel Niquet,[3,4] Diana Car,[5] Sebastien R. Plissard,[6] Walter Escoffier,[1] Erik P. A. M. Bakkers,[5] Ivan Duchemin,[3,4] Bertrand Raquet,[1] and Michel Goiran[1]

[1]*LNCMI-EMFL, INSA,UPS, UGA, CNRS-UPR3228, 143 Avenue de Rangueil, 31400 Toulouse, France*

[2]*QuTech and Kavli Institute of Nanoscience, Delft University of Technology, 2600 GA Delft, The Netherlands*

[3]*Université Grenoble Alpes, INAC-MEM, L_Sim, Grenoble, 38000 Grenoble, France*

[4]*CEA, INAC-MEM, L_Sim, 17 Rue des Martyrs, 38054 Grenoble, France*

[5]*Department of Applied Physics, Eindhoven University of Technology, 5600 MB Eindhoven, The Netherlands*

[6]*LAAS-CNRS, Université de Toulouse, CNRS, Toulouse, France*

(Received 5 July 2016; revised manuscript received 17 October 2016; published 5 December 2016)

The charge transport properties of individual InSb nanowires based transistors are studied at 4.2 K in the quasiballistic regime. The energy level separations at zero magnetic field are extracted from a bias voltage spectroscopy. The magnetoconductance under a magnetic field applied perpendicularly to the nanowire axis is investigated up to 50 T. Owing to the magnetic reduction of the backscattering, the electronic states of the quasi-one-dimensional electron gas are revealed by Landauer-Büttiker conductance quantization. The results are compared to theoretical predictions revealing the spin and orbital degeneracy lifting. At sufficiently high magnetic field the measurements show the evolution to the quantum Hall effect regime with the formation of Landau orbits and conducting edge states.

DOI: 10.1103/PhysRevB.94.235303

I. INTRODUCTION

Among all bulk semiconductors, InSb has the smallest band gap, $E_g = 0.017$ eV, the largest electronic mobility $\mu_e = 77\,000$ cm^2/(V-s) at room temperature [1], and benefits from a strong spin-orbit coupling associated with a high Landé factor $|g^*| = 51$ [2]. Owing to these properties, InSb nanowires (NWs) are promising objects for future nanoelectronic devices. For example, spin-filtering devices can be envisioned due to strong spin-orbit coupling leading to the formation of helical states [3–5]. They are also strongly involved in the search for Majorana fermions when coupled to superconducting leads [6–8]. As compared to bulk InSb, the charge carriers' confinement in one-dimensional (1D) NWs strongly affects the band structure with the formation of electrical subbands. Since a small band gap precludes any optical investigation, the band structure of InSb NWs remains largely unexplored and suffers from a lack of direct experimental investigations.

The energy levels can be probed through electronic transport in the ballistic regime. Indeed, band-structure information is obtained by analyzing the conductance in the frame of Landauer-Büttiker formalism. In addition to the successive conductance plateaus observed as the back-gate voltage is varied [9–11], a direct probe of the energy levels can be achieved using bias voltage spectroscopy, and compared with dedicated theoretical models [12–16].

The application of a strong enough magnetic field lifts the orbital and spin degeneracy of the electric subbands, providing additional knowledge of the band structure [11,17–19]. When the magnetic field is applied normal to the NW axis, the cyclotron diameter may become smaller than its NW counterpart. The device evolves towards a two-dimensional electron gas (2DEG) in the quantum Hall effect (QHE) regime where the spatial separation of the charge current associated with opposite momentum leads to a decrease in the backscattering [20–23].

II. EXPERIMENTAL METHODS

Transport measurements are performed on two InSb NW devices, named A and B, both having a diameter of $W = 100 \pm 5$ nm. The NWs are grown by metal-organic vapor phase epitaxy (MOVPE) on prepatterned InP substrates covered by arrays of gold islands. Prior to the InSb growth, InP-InAs stems are synthesized in order to improve the nucleation and to reduce the lattice mismatch. The NWs are positioned on a heavily p-doped Si/SiO$_2$ substrate using micromanipulators [24]. The thickness of the insulating SiO$_2$ is 285 nm. Such a substrate acts as a back gate, allowing control of the carrier concentration in the device through the application of a voltage V_g. The NWs are connected by two metallic electrodes (Ti/Au 5/145 nm) defined by electron beam lithography. They are deposited by evaporation after argon plasma etching. The channel length between the contacts L is 1 μm for device A and 600 nm for device B. More details concerning the device fabrication can be found in Refs. [25–27].

The samples are inserted in a ^{4}He cryostat and cooled down at 4.2 K. The two-probe conductance is investigated as a function of both bias and gate voltages by a standard lock-in amplifier technique. A bias voltage spectroscopy is realized by sweeping a dc bias (0–30 mV) voltage superimposed on an ac component of 0.5 mV$_{\rm rms}$ at a fixed gate voltage (in the 0–20 V range depending on the sample). The procedure is repeated for several electronic concentrations. The magnetoconductance is measured using an ac bias voltage of 1 mV$_{\rm rms}$ at a frequency around 1 kHz, under a pulsed magnetic field applied perpendicular to the NW axis, with a total duration of 0.3 s and up to 50 T [28].

 ©2016 American Physical Society

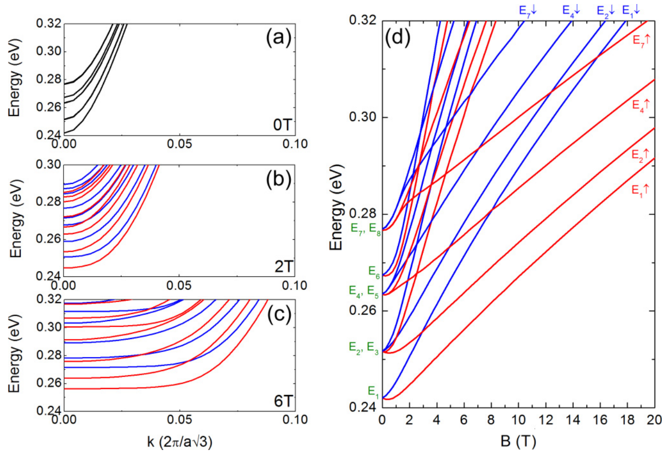

FIG. 1. Computed band structure of an InSb NW device. (a)–(c) Band structure for a magnetic field (a) $B = 0$ T, (b) $B = 2$ T, and (c) $B = 6$ T for, respectively, the top left, middle left, and bottom left graphs. a stands for the lattice parameter. (d) Bottom edge of the eight first subbands ($E_{1\text{–}8}$) as a function of the magnetic field. The two colors represent spin up and spin down.

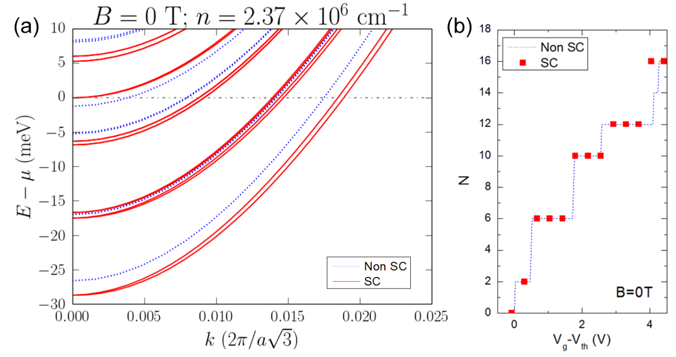

FIG. 2. (a) Comparison between the non-self-consistent (NSC) and self-consistent (SC) band structures at $B = 0$ T and carrier density $n = 2.37 \times 10^6$ cm^{-1} ($V_g - V_{\text{th}} \approx 2.9$ V). The zero of energy is the chemical potential μ. (b) Comparison between the number of occupied bands calculated at $B = 0$ T from the NSC, and from the SC band structures. The gate voltage is measured with respect to the threshold voltage V_{th}.

III. BAND-STRUCTURE SIMULATION

The electronic structure of a 100 nm diameter InSb NW was computed with a $sp^3d^5s^*$ model [29,30] including spin-orbit coupling. The band structure at zero magnetic and electric fields is plotted in Fig. 1(a) and its evolution under perpendicular magnetic fields in Figs. 1(b)–1(d).

The band structure evolves into magnetoelectric subbands as the field increases. The spin degeneracy is lifted by the Zeeman effect, which is particularly strong due to the high g^* factor. The orbital degeneracy is also lifted by the coupling of the electron orbital momentum with the magnetic field. The subbands tend towards nondispersive bulk states and dispersive edge states for small and large k vectors, respectively. Finally, the whole spectrum is shifted to higher energy due to diamagnetism. We extract from the simulation a g^* factor of 52.51 for the first subbands, and slightly lower values for higher modes. This result is in line with previous studies reporting an exceptionally high g^* factor and strong spin-orbit coupling in confined InSb based systems, such has NWs [14,31], quantum dots [32–34], and quantum point contacts [32–34], at least for the first subbands.

Since the carrier population is controlled by a back gate, it is important to understand how the electric field and the electron-electron interactions act upon the band structure and conductance. We have, therefore, performed self-consistent tight-binding calculations of the band structure of infinitely long NWs lying on a 285 nm thick SiO_2 layer. The electron-electron interactions are treated in the mean-field (Schrödinger-Poisson) approximation [35].

Figure 2(a) compares the non-self-consistent (NSC) and self-consistent (SC) band structures at $B = 0$ T for a given density while Fig. 2(b) shows the number of occupied subbands computed versus gate voltage. The capacitance extracted from the SC simulations, $C \approx 39$ pF/m, is significantly larger than the experimental one (estimated ≈ 11 pF/m in the next section), but close to the geometrical capacitance $C \approx 45$ pF/m of a metallic NW. The mismatch between the calculated and experimental capacitances likely results from finite size effects (the ratio between the length of the NWs and the thickness of the oxide being relatively small) and the electrostatic screening of the contacts. This is frequently observed for NWs [11,36,37]. We have therefore scaled the gate voltage axis in Fig. 2(b) by a factor 39/11 in order to match the experimental capacitance. Alternatively, we have verified that similar results are obtained when we mimic the experimental capacitance in the self-consistent simulations by decreasing the dielectric constant of the oxide.

Figure 2 demonstrates that the electric field has little influence on the position and the width of the first few conductance plateaus at $B = 0$ T. The impact of the electric field is larger at high magnetic field, but remains reasonable for the low capacitances measured experimentally. The NSC band structures can therefore provide the main guidelines for the interpretation of the experimental data. For larger capacitances however, the $E_4\uparrow$ and $E_1\downarrow$ bands might get closer and cross at larger magnetic fields.

IV. BIAS VOLTAGE SPECTROSCOPY

For a 1D conductor in the quasiballistic regime, the conductance is expressed, in the Landauer-Büttiker formalism, as the sum over all occupied subbands of G_0Tr [21]. $G_0 = 2e^2/h$ is the spin degenerate quantum of conductance and Tr the transmission coefficient of the subbands. The conductance is measured versus bias voltage for different gate voltages increasing by steps of $\Delta V_g = 0.2$ V. In Fig. 3(a), the curves tend to converge at the plateaus since the conductance is nearly constant between two successive V_g steps. The low bias conductance versus gate voltage $G(V_g)$ is extracted and plotted in Fig. 3(b). The monotonous increase of $G(V_g)$ is punctuated by plateaus together with strong fluctuations. We are not able to determine the exact nature of these fluctuations, either due to universal conductance fluctuations or Fabry-Pérot oscillations because of the large step value.

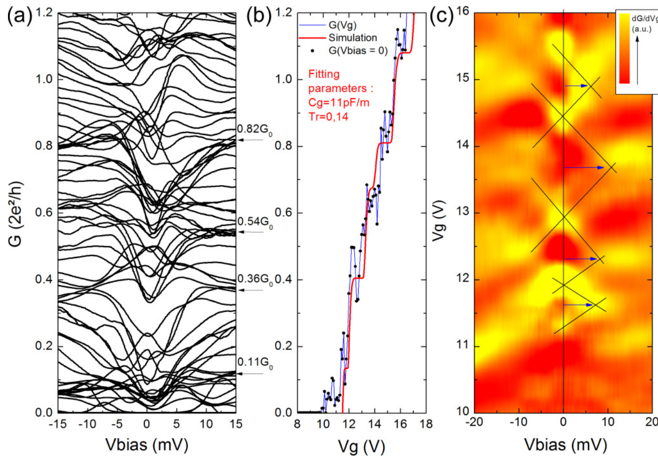

FIG. 3. Bias voltage spectroscopy performed on device A at 4.2 K. (a) Conductance vs bias voltage for a set of gate voltages from 8 to 18 V in steps of 0.2 V. (b) Transfer characteristic (blue) at low bias interpolated from the data of (a) superimposed with conductance simulation (red). The low bias conductance of each curve in (a) is represented by black points. (c) Color plot of the transconductance $\partial G/\partial V_g$ derived from data in (a). Black lines are guides for the eyes to follow the evolution of the transconductance maxima in yellow.

At finite bias voltages, as the energy window defined by V_{bias} exceeds the subband energy spacing, conductance plateaus evolve towards so-called "half plateaus" at intermediate conductance values [13,14,16]. We find clear evidence of the formation of the half plateaus in Fig. 3(a). At high bias, quantum interferences are suppressed due to the electron-electron scattering [21,38,39].

The transconductance $\partial G/\partial V_g$ was numerically derived from the data depicted in Fig. 3(a) and is shown in the color plot in Fig. 3(c). Transconductance maxima appear between successive plateaus corresponding to the alignment of the Fermi energy with the bottom of each subband. As the bias voltage is increased, adjacent transconductance maxima merge, forming a checkerboard pattern. The intersection gives an estimate of the energy difference $\Delta E = eV_{\text{bias}}$ between the two involved subbands [14]. The results, summarized in Table I, are in reasonable agreement with the simulated NSC band structure for the two lower subbands and slightly different for the two immediately above. The discrepancy might be attributed to the effect of electric field on the subband energy, as explained previously.

The corresponding theoretical Landauer-Büttiker conductance in the absence of quantum interferences is calculated in order to fit the experimental results using the calculated band structure [11]. The result is plotted on the $G(V_g)$ graph

TABLE I. Energy splittings for the five first degenerate subbands.

ΔE	Computed (meV)	Measured (meV)
$E_1 - (E_2,E_3)$	9.6	7.5 ± 3
$(E_2,E_3) - (E_4,E_5)$	11.7	8 ± 3
$(E_4,E_5) - E_6$	4	10 ± 3
$E_6 - (E_7,E_8)$	9.3	6 ± 3

[Fig. 3(b)] together with the experimental curve. The gate coupling C_g and the transmission coefficients Tr are set as free parameters. A good agreement was found for $C_g = 11$ pF/m and Tr = 0.14.

V. MAGNETOTRANSPORT SPECTROSCOPY

In the following, we shall focus on sample B, which shows similar results as sample A but with greater experimental resolution. The transfer characteristics and its temperature dependence are reproduced in Fig. 4(a). The low temperature magnetoconductance $G(B)$ is plotted in Fig. 4(b) for several gate voltage values. It mainly shows a decreasing behavior together with different features depending on the field range. Additional measurements of the magnetoconductance (not shown here) from $V_g = 2.5$ to 10 V in steps of 0.5 V were performed to interpolate the $G(V_g)$ characteristic in a magnetic field range from 0 to 26 T in Fig. 4(c). From 0 to 5 T, weak conductance modulations are observed on $G(B)$. Above 5 T, the fall of the conductance is punctuated by clear plateaus at 0.3-0.6-1.3-1.6G_0. These plateaus are also visible in the interpolated $G(V_g)$ curves. As the magnetic field is swept, the different subbands rise progressively above the Fermi energy, reducing the number of conducting channels and the conductance thus decreasing stepwise [11,40].

The well-defined conductance plateaus at integer multiples of 0.3G_0 (except at 0.9G_0, as explained later) above 5 T

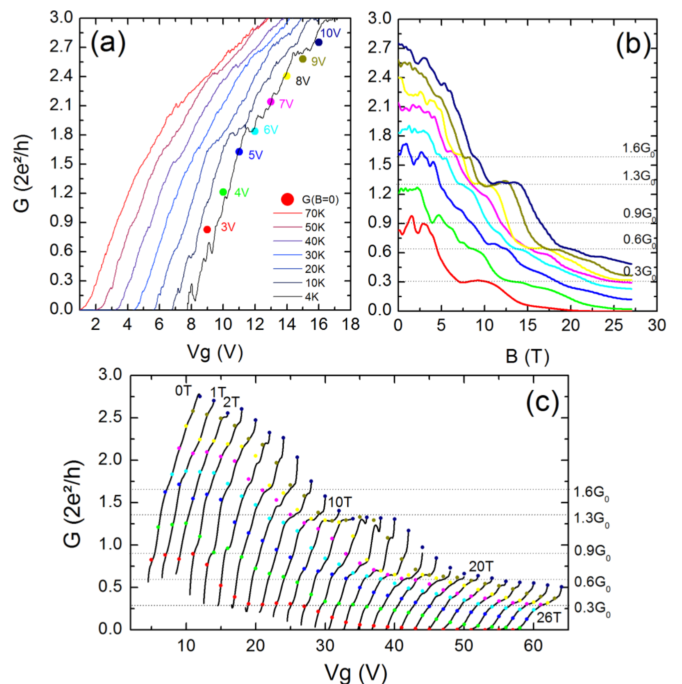

FIG. 4. Transport measurement of device B. (a) Temperature dependence of the transfer characteristic at zero magnetic field. An offset on V_g is added for clarity. (b) Conductance vs magnetic field for a few gate voltages corresponding to the colored points in (a) at 4.2 K. (c) Evolution of the transfer characteristic with magnetic field from 0 to 26 T at 4.2 K interpolated from $G(B)$ measurements. The color points are the experimental values. An offset on V_g is added for clarity.

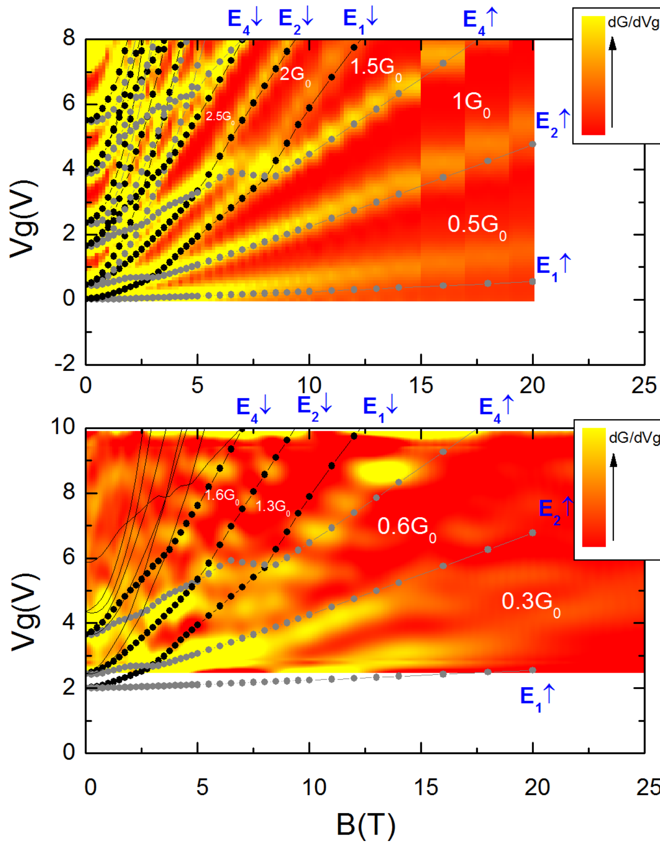

FIG. 5. Color plot of the transconductance $\partial G/\partial V_g$ vs gate voltage and magnetic field calculated (NSC) for a ballistic conductor (top) and obtained from the experimental results (bottom) of device A. The maxima of transconductance appear in yellow. The coordinates where the simulated Fermi energy crosses the bottom of each subband is calculated and plotted in black and gray curves according to the spin state considering a gate coupling of 13 pF/m. The subbands are indexed $E_{1\text{–}4}\uparrow\downarrow$ according to the subband number in Fig. 4 and the spin state.

suggest a strong reduction of the backscattering, leading to ballistic transport. The observed conductance plateaus do not coincide with integer multiples of $(e^2/h) = 0.5G_0$. The difference between the pure ballistic plateau sequence and the experimental results is usually attributed to the contact resistance in series with the NW.

A convenient way to evidence the signatures of the band structure in magnetoconductance measurements is to plot the transcondutance $\partial G/\partial V_g$ as a function of both the gate voltage and the magnetic field in Fig. 5. As already mentioned, a transconductance maximum appears as the Fermi energy is aligned with the bottom of a subband. Transconductance maxima (yellow shaded areas) condensate in clear structures that rise as the magnetic field is swept. The splitting of the maxima for increasing magnetic field is the signature of the degeneracy lifting together with the subband flattening.

From the band-structure simulation in Fig. 1 we computed the (B,V_g) coordinates where the Fermi energy is aligned with the bottom of each subband. They are superimposed to the transconductance color plot of Fig. 5. A very good agreement between the transconductance maxima and the subbands (B,V_g) coordinates is obtained for the unique fitting parameter $C_g = 13$ pF/m. This value is very close to the one obtained from bias voltage spectroscopy of device A in Fig. 3. A broad transconductance maxima between the $0.6G_0$ and $1.3G_0$ plateaus lie in between the (B,V_g) coordinates of $E_1\downarrow$ and $E_4\uparrow$. Self-consistent simulations of the band structure at high field suggest a lower energy difference between these subbands, resulting in a single transconductance maximum trace. This situation explains the "missing conductance plateau" expected at $0.9G_0$ in Figs. 4(b) and 4(c).

Finally, at high magnetic field, the conductance drops towards zero. Assuming a constant carrier density, the Fermi level is pinned on the lowest subband and one should observe a constant conductance value of $G = \mathrm{Tr}(e^2/h)$. The diamagnetic shift of the lowest subband ultimately collapses the quantum capacitance. This effect is not taken into account in the simulation. For low gate voltages, the quantum capacitance lowers the total capacitance, resulting in the canal depletion [41,42].

VI. MAGNETOTRANSPORT THROUGH BALLISTIC EDGE STATES

In similar studies, a resistance of few kΩ associated with the contact resistance is subtracted to the conductance curves [14,27,43]. In this work, we consider a transmission probability at the interface between the metallic pads and the NW. The total transmission $\mathrm{Tr}_{\mathrm{tot}}$ is the product of the channel transmission $\mathrm{Tr}_{\mathrm{ch}}$ with the contact transmission $\mathrm{Tr}_{\mathrm{co}}$. In contrast to the expected conductance plateaus at 0.5-1-2-2.5G_0, the experimental plateaus at 0.3-0.6-1.3-1.6G_0 are explained by considering a contact transmission coefficient of $\mathrm{Tr}_{\mathrm{co}} = 0.65$.

Assuming that the transmission at the contact is independent of the magnetic field, the value of the channel transmission $\mathrm{Tr}_{\mathrm{ch}} = \mathrm{Tr}_{\mathrm{tot}}/\mathrm{Tr}_{\mathrm{co}}$ at $B = 0$ T is found to be around 0.23. The corresponding mean free path $\ell = 180$ nm is deduced from the relation $\mathrm{Tr}_{\mathrm{ch}} = \ell/(L+\ell)$. This value is larger than the diameter of the NW and a few times smaller than its channel length, in agreement with the quasiballistic regime.

The conductance plateaus allow a precise investigation of the charge transport evolution. As the cyclotron diameter of the Landau state n, $d_c = 2(2n+1)^{1/2}\ell_B$ (with $\ell_B = \sqrt{\hbar/eB}$ the magnetic length and h the reduced Planck constant) becomes smaller than the NW diameter, the magnetic confinement overcomes the electronic confinement and the subbands start to form well-defined Landau states [20,21]. The electron gas tends to behave as a 2D gas in the QHE regime. The number of occupied Landau levels (or filling factor) $\nu = (h/eB)N_e^{2D}$ is linear with $1/B$ until the cyclotron radius becomes comparable to the width of the channel [40,44–47].

The conductance is measured up to 50 T for a gate voltage $V_g = 8$ V corresponding to around ten occupied spin degenerate subbands at 0 T. The filling factor as a function of the reciprocal magnetic field is reported in Fig. 6. The number of occupied channels follows a linear behavior above a critical field of approximately 7 T. Deviation from linearity starts at the crossover between the 1D and the QHE regime. An effective 2DEG carrier density is computed by dividing the number of electrons C_gV_g/e by $L\cdot W$ with $L = 600$ nm. A

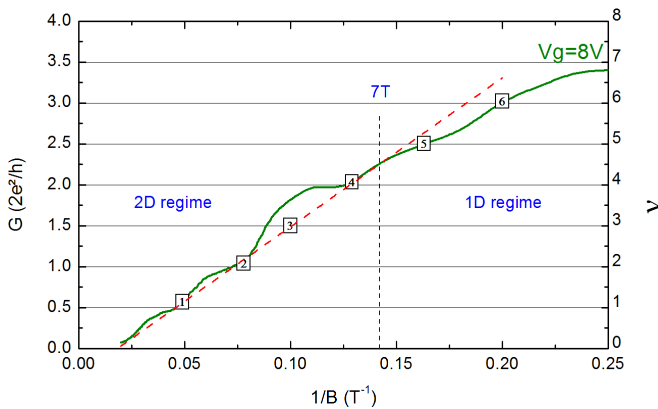

FIG. 6. Conductance and filling factor vs $1/B$ measured from 0 to 50 T at 4.2 K for a gate voltage of $V_g = 8$ V. The conductance increase between two plateaus reveals the occupation of one additional subband. The number of occupied subbands is given in the open squares. In order to take the contact transmission into account, a reflexion coefficient of 0.35 was removed.

gate coupling of $C_g = 13$ pF/m is considered. An agreement is found between the curve in Fig. 6, and the theoretical formula with a width W around 66 ± 3 nm. This estimation is close to the observed diameter of 100 nm. Hall effect measurements have already been reported in InP core-shell NW by Storm *et al.* [48] and in InAs NW by Blömers *et al.* [49] using local probes on devices with widths around 200 nm. In contrast, the result presented here is evidence of the QHE regime in a NW, highlighting the specific transport properties under high magnetic field.

VII. CONCLUSION

The 1D conducting modes of individual InSb NWs are investigated by conductance measurements at low temperature and under large magnetic fields oriented perpendicularly to the nanowire axis. Bias voltage spectroscopy gives direct estimation of the subband energy difference between the few first subbands at zero magnetic fields. The results are in relatively good agreement with the band-structure simulation. Magnetoconductance measurements show signatures of nondegenerate subbands. They are well reproduced by the band-structure simulation taking into account the Zeeman splitting, the orbital degeneracy lifting, and the diamagnetism shift of the 1D electronic modes. The perpendicular high magnetic field reveals 2D-like Landau levels characterized by conducting edge states that suppress the backscattering.

ACKNOWLEDGMENTS

High magnetic field measurements were performed at LNCMI under the EMFL proposal TSC10-213. Parts of the calculations were run on the CCRT/Curie machine using allocations from GENCI.

[1] D. L. Rode, Phys. Rev. B **3**, 3287 (1971).
[2] R. A. Isaacson, Phys. Rev. **169**, 312 (1968).
[3] P. Středa and P. Šeba, Phys. Rev. Lett. **90**, 256601 (2003).
[4] C. H. L. Quay, T. L. Hughes, J. A. Sulpizio, L. N. Pfeiffer, L. N. Pfeiffer, K. W. Baldwin, K. W. West, D. Goldhaber-Gordon, and R. de Picciotto, Nat. Phys. **6**, 336 (2010).
[5] S. Datta and B. Das, Appl. Phys. Lett. **56** 665 (1990).
[6] V. Mourik, K. Zuo, S. M. Frolov, S. R. Plissard, E. P. A. M. Bakkers, and L. P. Kouwenhoven, Science **336**, 1003 (2012).
[7] M. T. Deng, C. L. Yu, G. Y. Huang, M. Larsson, P. Caroff, and H. Q. Xu, Nano Lett. **12**, 6414 (2012).
[8] M. T. Deng, C. L. Yu, G. Y. Huang, M. Larsson, P. Caroff, and H. Q. Xu, Sci. Rep. **4**, 7261 (2014).
[9] S. Chuang, Q. Gao, R. Kapadia, A. C. Ford, J. Guo, and A. Javey, Nano Lett. **13**, 555 (2013).
[10] A. C. Ford, S. B. Kumar, R. Kapadia, J. Guo, and A. Javey, Nano Lett. **12**, 1340 (2012).
[11] F. Vigneau, V. Prudkovkiy, I. Duchemin, W. Escoffier, P. Caroff, Y.-M. Niquet, R. Leturcq, M. Goiran, and B. Raquet, Phys. Rev. Lett. **112**, 076801 (2014).
[12] L. I. Glazman and A. V. Khaetskii, JETP Lett. **48**, 591 (1998).
[13] L. P. Kouwenhoven, B. J. van Wees, C. J. P. M. Harmans, J. G. Williamson, H. van Houten, C. W. J. Beenakker, C. T. Foxon, and J. J. Harris, Phys. Rev. B **39**, 8040 (1989).
[14] I. van Weperen, O. Gul, S. R. Plissard, E. P. A. M. Bakkers, S. M. Frolov, and L. P. Kouwenhoven, Nano Lett. **13**, 387 (2013).
[15] W. Lu, J. Xiang, B. P. Timko, Y. Wu, and C. M. Lieber, Proc. Natl. Acad. Sci. USA **102**, 10046 (2005).
[16] N. K. Patel, J. T. Nicholls, L. Martin-Moreno, M. Pepper, J. E. F. Frost, D. A. Ritchie, and G. A. C. Jones, Phys. Rev. B **44**, 13549 (1991).
[17] G. W. Holloway, D. Shiri, C. M. Haapamaki, K. Willick, G. Watson, R. R. LaPierre, and J. Baugh, Phys. Rev. B **91**, 045422 (2015).
[18] S. Heedt, W. Prost, J. Schubert, D. Grützmacher, and T. Schäpers, Nano Lett. **16**, 3116 (2016).
[19] J. Kammhuber, M. C. Cassidy, H. Zhang, Önder Gül, F. Pei, M. W. A. de Moor, B. Nijholt, K. Watanabe, T. Taniguchi, D. Car, S. R. Plissard, E. P. A. M. Bakkers, and L. P. Kouwenhoven, Nano Lett. **16**, 3482 (2016).
[20] C. Beenakker, H. Houten, and B. Wees, Superlattices Microstruct. **5**, 127 (1989).
[21] C. W. J. Beenakker and H. van Houten, Solid State Phys. **44**, 1 (1991).
[22] M. Büttiker, Phys. Rev. B **38**, 9375 (1988).
[23] H. van Houten, C. W. J. Beenakker, P. H. M. van Loosdrecht, T. J. Thornton, H. Ahmed, M. Pepper, C. T. Foxon, and J. J. Harris, Phys. Rev. B **37**, 8534 (1988).
[24] K. Flöhr, M. Liebmann, K. Sladek, H. Y. Günel, R. Frielinghaus, F. Haas, C. Meyer, H. Hardtdegen, T. Schäpers, D. Grützmacher, and M. Morgenstern, Rev. Sci. Instrum. **82**, 113705 (2011).
[25] D. Car, J. Wang, M. A. Verheijen, E. P. A. M. Bakkers, and S. R. Plissard, Adv. Mater. **26**, 4875 (2014).

[26] S. R. Plissard, D. R. Slapak, M. A. Verheijen, M. Hocevar, G. W. G. Immink, I. van Weperen, S. Nadj-Perge, S. M. Frolov, L. P. Kouwenhoven, and E. P. A. M. Bakkers, Nano Lett. **12**, 1794 (2012).

[27] O. Gul, D. J. van Woerkom, I. van Weperen, D. Car, S. R. Plissard, E. P. A. M. Bakkers, and L. P. Kouwenhoven, Nanotechnology **26**, 215202 (2015).

[28] F. Debray and P. Frings, C. R. Phys. **14**, 2 (2013).

[29] Y. M. Niquet, A. Lherbier, N. H. Quang, M. V. Fernández-Serra, X. Blase, and C. Delerue, Phys. Rev. B **73**, 165319 (2006).

[30] J.-M. Jancu, R. Scholz, F. Beltram, and F. Bassani, Phys. Rev. B **57**, 6493 (1998).

[31] I. van Weperen, B. Tarasinski, D. Eeltink, V. S. Pribiag, S. R. Plissard, E. P. A. M. Bakkers, L. P. Kouwenhoven, and M. Wimmer, Phys. Rev. B **91**, 201413 (2015).

[32] S. Nadj-Perge, V. S. Pribiag, J. W. G. van den Berg, K. Zuo, S. R. Plissard, E. P. A. M. Bakkers, S. M. Frolov, and L. P. Kouwenhoven, Phys. Rev. Lett. **108**, 166801 (2012).

[33] H. A. Nilsson, P. P. Caroff, C. Thelander, M. Larsson, J. B. Wagner, L.-E. Wernersson, L. Samuelson, and H. Q. Xu, Nano Lett. **9**, 3151 (2009).

[34] V. S. Pribiag, S. Nadj-Perge, S. M. Frolov, J. W. G. van den Berg, I. van Weperen, B. E. P. A. M. Plissard, S. R. and, and L. P. Kouwenhoven, Nat. Nanotechnol. **8**, 170 (2013).

[35] E. Lind, Y.-M. Niquet, H. Mera, and L.-E. Wernersson, Appl. Phys. Lett. **96**, 233507 (2010).

[36] A. C. Ford, J. C. Ho, Y.-L. Chueh, Y.-C. Tseng, Z. Fan, J. Guo, J. Bokor, and A. Javey, Nano Lett. **9**, 360 (2009).

[37] A. V. Kretinin, R. Popovitz-Biro, D. Mahalu, and H. Shtrikman, Nano Lett. **10**, 3439 (2010).

[38] T. Ludwig, Y. M. Blanter, and A. D. Mirlin, Phys. Rev. B **70**, 235315 (2004).

[39] B. L. Altshuler, A. G. Aronov, and D. E. Khmelnitsky, J. Phys. C **15**, 7367 (1982).

[40] K. F. Berggren, T. J. Thornton, D. J. Newson, and M. Pepper, Phys. Rev. Lett. **57**, 1769 (1986).

[41] S. Ilani, L. A. Donev, M. Kindermann, and P. L. McEuen, Nat. Phys. **2**, 687 (2006).

[42] M. Krüger, M. R. Buitelaar, T. Nussbaumer, C. Schönenberger, and L. Forró, Appl. Phys. Lett. **78**, 1291 (2001).

[43] M. de la Mata, R. Leturcq, S. R. Plissard, C. Rolland, C. Magén, J. Arbiol, and P. Caroff, Nano Lett. **16**, 825 (2016).

[44] K.-F. Berggren, G. Roos, and H. van Houten, Phys. Rev. B **37**, 10118 (1988).

[45] B. J. van Wees, L. P. Kouwenhoven, E. M. M. Willems, C. J. P. M. Harmans, J. E. Mooij, H. van Houten, C. W. J. Beenakker, J. G. Williamson, and C. T. Foxon, Phys. Rev. B **43**, 12431 (1991).

[46] H. van Houten, B. van Wees, J. Mooij, G. Roos, and K.-F. Berggren, Superlattices Microstruct. **3**, 497 (1987).

[47] R. Ribeiro, J.-M. Poumirol, A. Cresti, W. Escoffier, M. Goiran, J.-M. Broto, S. Roche, and B. Raquet, Phys. Rev. Lett. **107**, 086601 (2011).

[48] K. Storm, F. Halvardsson, M. Heurlin, D. Lindgren, A. Gustafsson, P. M. Wu, B. Monemar, and L. Samuelson, Nat. Nanotechnol. **7**, 718 (2012).

[49] C. Blömers, T. Grap, M. I. Lepsa, J. Moers, S. Trellenkamp, D. Grützmacher, H. Lüth, and T. Schäpers, Appl. Phys. Lett. **101**, 152106 (2012).